Additive Manufacturing 34 (2020) 101367

Contents lists available at ScienceDirect

Additive Manufacturing

journal homepage: www.elsevier.com/locate/addma

Light based synthesis of metallic nanoparticles on surface-modified 3D printed substrates for high performance electronic systems

Reza N. Esfahani[a], Matthew P. Shuttleworth[a], Viktor Doychinov[b], Nathan J. Wilkinson[a], Jack Hinton[a], Tom D.A. Jones[c], Assel Ryspayeva[c], Ian D. Robertson[b], Jose Marques-Hueso[c], Marc. P.Y. Desmulliez[c], Russell A. Harris[a], Robert W. Kay[a,*]

[a] Future Manufacturing Processes Research Group (FMPRG), School of Mechanical Engineering, University of Leeds, LS2 9JT, United Kingdom
[b] Institute of Robotics, Autonomous Systems, and Sensing, School of Electronic and Electrical Engineering, University of Leeds, LS2 9JT, United Kingdom
[c] School of Engineering & Physical Sciences, Nature Inspired Manufacturing Centre (NIMC), Heriot-Watt University, EH14 4AS, United Kingdom

ARTICLE INFO

Keywords:
Polyetherimide
Surface-modified polymer
Light-based patterning
Personalised electronics
Wireless communications
Shape memory alloy

ABSTRACT

Additive Manufacturing is capable of producing highly complex and personalised products. However, innovation in both material science and processing is required to achieve the performance, reliability and miniaturization of modern mass-produced electronic systems. This article presents a new digital fabrication strategy that combines 3D printing of high-performance polymers (polyetherimide) with light-based selective metallisation of copper traces through chemical modification of the polymer surface, and computer-controlled assembly of functional devices and structures. Using this approach, precise and robust conductive circuitry is fabricated across flexible and conformal surfaces omitting the need to connect and assemble separate circuits. To show how this process is compatible with existing electronic packaging techniques a range of modern components are solder surface mount assembled to selectively metalized bond pads. To highlight the potential applications stemming from this new capability, high frequency wireless communications, inductive powering and positional sensing demonstrators are manufactured and characterised. Furthermore, the incorporation of actuation is achieved through selective heating of shape memory alloys with a view towards routes towards folding and deployable 3D electronic systems. The results in this paper show how this process provides the required mechanical, electrical, thermal and electromagnetic properties for future real-world applications in the field of robotics, medicine, and wearable technologies.

1. Introduction

Electronics manufacturing research using 3D digitally driven fabrication techniques such as Additive Manufacturing offers a route to creating highly customized devices [1–3]. Research is focused on techniques capable of depositing conductive materials to create circuitry on a dielectric substrate. Various avenues are being explored by either direct 3D printing using multiple deposition heads [4–7] or combining additive manufacturing with secondary computer controlled processes such as dispensing [8,9], ink jet printing [10,11], aerosol jetting [12,13], wire embedding [14,15], laser direct structuring [16] and metal injection [17–19] to functionalise the part. However, to match the capabilities of existing PCB manufacture, alternative 3D printable insulator materials are needed that can provide enhanced dielectric, thermal and mechanical performance. Furthermore, advancements in generating conductor layers with a finer resolution, improved electrical properties and stronger adhesion are required. Another critical limitation for the fabrication of electronic systems using 3D printing approaches is the methods for attaching componentry to the circuitry. Due to the low heat deflection of the insulator material, or the poor solderability of the conductor material, existing techniques have relied on bonding using conductive adhesives [7–9,12] or other low temperature joining materials [6,17,18]. These materials do not require high temperature thermal processing but typically do not form the same metallurgical contact as solder, which partially diffuses into the metal bond pad to form a reliable low resistance attachment between the electronic components [20]. Recent work has shown the potential for soldering to Cu coated 3D printed structures, however, the underlying low melt temperature of the insulator layer limits practical applications [21,22]. This paper presents a new hybrid additive manufacturing strategy that overcomes all the aforementioned challenges providing a route to fabricate personalised high-performance 3D

* Corresponding author.
E-mail address: r.w.kay@leeds.ac.uk (R.W. Kay).

https://doi.org/10.1016/j.addma.2020.101367
Received 18 March 2020; Received in revised form 18 May 2020; Accepted 31 May 2020
Available online 15 June 2020

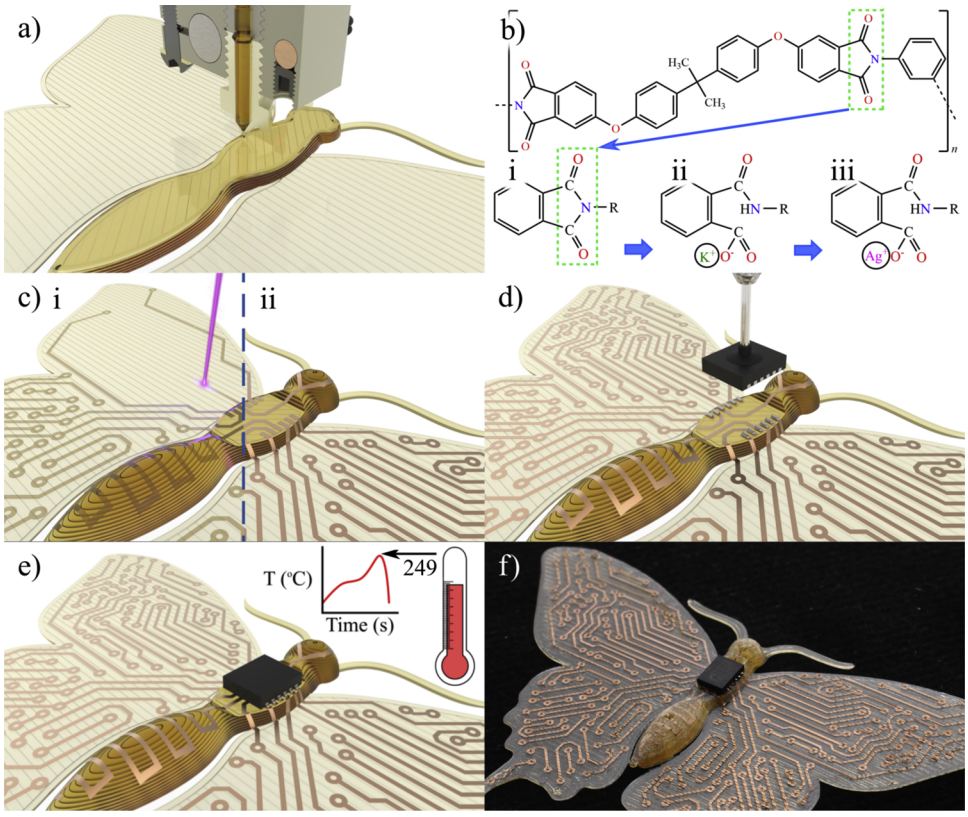

Fig. 1. Graphical schematic of the digitally driven fabrication process **(a)** Fused Filament Fabrication of PEI substrate. **(b)** Surface chemical modification of **(i)** functional imide structure. **(ii)** Hydrolysis to cleave imide ring, **(iii)** ion exchange to form silver polyamate. **(c)** Metal patterning via **(i)** selective UV laser irradiation inducing Ag nanoparticles, **(ii)** electroless copper plating. **(d)** Computer controlled solder paste dispensing and surface mount assembly of electronic components. **(e)** Solder reflow. **(f)** Demonstrator manufactured using this technique.

electronic systems.

2. Process description

2.1. Process overview

The process begins with 3D printing a polyetherimide (PEI) based filament (ULTEM 1010) using a Fused Filament Fabrication (FFF) process whereby molten PEI is selectively extruded from a nozzle layer-by-layer to build a 3D geometry (Fig. 1a). PEI based materials are amorphous, thermoplastic polymers that can be 3D printed, are chemically stable, biocompatible and exhibit the mechanical, thermal, and dielectric properties required for next generation applications. A low-cost table-top printer is used that has been modified to accommodate the higher printing temperatures required to deposit this material. The second stage of the process involves selectively metalizing the PEI surface using an electroless plating process initiated by the localized photoreduction of metallic nanoparticles. This is achieved by chemically modifying the polymer's imide component (Fig. 1b-i) using a two-stage reaction involving an alkaline hydrolysis using potassium hydroxide (KOH) to form potassium polyamate (Fig. 1b-ii) then a subsequent ion exchange through immersion in silver nitrate (AgNO3) to form silver polyamate (Fig. 1b-iii). Upon exposure to 405 nm light the silver ions are reduced through photolysis to synthesise metallic nanoparticles in the order of 20–70 nm [23–25] (Fig. 1c–i). Any unexposed residual silver ions are then removed to allow the remaining silver nanoparticles to act as a seed site for an electroless copper deposition using a tartrate-based solution (Fig. 1c-ii). The final part of the process involves the incorporation of additional functionality using computer-controlled dispensing and robotic pick-and-place assembly (Fig. 1d). Unlike common 3D printed filaments, such as ABS, PLA and PC, this research shows that ULTEM 1010 can withstand a solder reflow process (Fig. 1e). Further incorporation of actuation is achieved by embedding shape memory alloy wire within the printed part. To showcase the freeform nature of this process a 3D butterfly shape is fabricated with a wingspan of 59 mm containing flexible and conformal circuitry (Fig. 1f). Previous research by the authors has systematically developed the material chemistry and resultant Ag formation using analytical techniques including; Fourier transform, infrared spectra, transmission electron microscopy, x-ray diffraction, and energy dispersive x-ray analysis, including the production of a 3D printed planar demonstrator using a photomask [26].

2.2. Fused filament fabrication

1.75 mm diameter PEI based ULTEM filament (1010, 3DXTech) was printed on a low-cost FFF 3D printer (K8200, Velleman). The machine was modified to accommodate the higher printing temperatures required for the PEI material through the addition of an all-metal hotend (V6, E3D) and a 12.5 kW/m^2 silicone heater mat (Keenovo). A 3 mm thick cast borosilicate glass plate (Ooznest) was placed over the heater mat and covered with 100 mm wide Kapton tape (Cadillac Plastics) to provide a flat surface and improve the part adhesion during printing. The 3D models were designed in Solidworks (Solidworks 2017, Dassault Systèmes) and prepared for 3D printing using an open-source slicer (Slic3r). Parts were deposited using a 0.3 mm dimeter nozzle (Plated Copper Nozzle, E3D), 0.45 μm layer thickness, 360 °C extrusion temperature and 200 °C build plate temperature.

2.3. Light based synthesis of silver nanoparticles

The surface of the 3D printed ULTEM substrates were chemically modified using a two-stage chemical dip. Firstly, 15 M potassium hydroxide (Across Organics) at 80 °C for 30 min to cleave the functional imide ring followed by 0.1 N silver nitrate at ambient temperatures (Across Organics) for 15 min to perform the ion exchange. Ag nanoparticles were selectively synthesised using a re-purposed stereolithography printer (Form 1+ with Open FL, FormLabs). This system uses a 120mw GaN laser diode and a x-y axis 20kpps galvanometer scanner to digitally control the laser spot position. In order to align

samples prior to exposure a 3D printed jig ensured repeatable placement of the substrate. Using a 62 mW power setting, 60 mm/s write speed the areas to be functionalised were scanned multiple times to achieve an overall 350 J/cm^2 irradiation. After laser patterning, samples were dipped for 10 s into 17.5 % ammonium hydroxide (Fisher Scientific) followed by 20 s in 1 M sulphuric acid (Fisher Scientific) to remove any residual silver ions. The optical power output of the laser beam is measured using a Thorlabs S310C sensor (Thorlabs UK).

Circuit designs were produced in EAGLE (EAGLE 9.2.1, Autodesk) and exported as DXF file format. These design files were then imported into Solidworks (Solidworks 2017, Dassault Systèmes) and converted to a 3D model which was then outputted as an STL file.

2.4. Electroless copper plating

The selectively silver seeded substrates were placed into a 300 mL glass beaker containing a tartrate based electroless copper plating bath (METEX 9962, MacDermid Enthone) for 40 min. Formaldehyde HCHO was the reducing agent with a 3.78 g/L copper (II) sulfate and 14 g/L sodium hydroxide content, a HCHO/Cu mass ratio of, 2.24 and pH 13. A digital magnetic stirring hotplate (AREC.X, Velp Scientifica) maintained a bath temperature of 40 °C and solution agitation at 200 rpm.

2.5. Component assembly

Solder deposition and component placement was performed using a 3-axis benchtop dispensing robot (F7400NVL, Fisnar). Two Type-5 solder pastes were trialed, Sn96.5-Ag3-Cu0.5 (SMD4300SNL10T5, Chip Quik) and Sn42-Bi57.6-Ag0.4 (TS391LT, Chipquik). Solder was dispensed using a luer lock nozzle (27-gauge tapered, Fisnar). Solder reflow was performed in a convection oven (LHT6030, Carbolite) preheated to 100 °C prior to loading the part. The temperature was then ramped to 249 °C which took around 6 min and held at a peak temperature for 1 min. Parts were then rapidly cooled by removal from the oven and any flux residues cleaned using isopropanol (Fisher Scientific). Oven temperature was monitored using a K-Type thermocouple connected to a benchtop multimeter (2110 5½ Digit, Keithley).

2.6. Actuation

0.5 mm diameter Nitinol wire (SmartFlex, SAES Getters) was held in a straight position and placed into an oven (LHT6030, Carbolite) at 550 °C for 45 min. Wire was quenched in cold water immediately after removal from the oven. 3D printing allows pre-fabricated apertures to be formed, into which the wire was then manually threaded. This stage of the process could later be automated and conducted during the printing process.

3. Methods

3.1. Imaging and videography

Photos and videos were captured on a DSLR Camera (D7500, Nikon) with 18 − 140 mm zoom and 50 mm macro lenses. Close-up 3D imaging of the circuitry across the layers was captured using a digital microscope (VHX-6000 Series, Keyence). No image post-processing was conducted except for white balance correction and cropping images to size.

3.2. Geometric characterization

Optical microscopy measurements (BX53 M, Olympus) were performed using 2×, 5× and 10× planar corrected lens (UIS-2, Olympus). Ag microstructures were analysed (Appendix A, Fig. A1) using a Field Emission Scanning Electron Microscope (1530, LEO). Surface profile and thickness measurements were taken using a white light interferometer at 10× magnification (NP FLEX, Bruker). Further details of the thickness measurements are shown in Appendix A, Table A1.

3.3. Conductivity measurement

Conductivity was measured using a 4-point probe (1 mm Spacing, 60 g, TC, Tip Rμ 100, Jandel Engineering Ltd.) connected to a sourcemeter unit (2450, Keithley). The test specimen was a 20 mm circle of copper plated onto a 30 × 30 × 1 mm ULTEM 1010 Substrate. Measurements were taken using a 100 mA source current at 10 separate locations across the sample. Finally, a correction factor of 0.9788 was applied to account for the samples diameter compared with the probe spacing before the results were averaged and multiplied by the thickness to obtain the bulk conductivity.

3.4. RF simulation

The antennas were designed and simulated using ANSYS (HFSS 2017, ANSYS), in a driven modal solution setup, with a perfectly matched layers radiation boundary condition. The antennas were excited using a wave port, renormalized to a 50Ω characteristic impedance. The copper surfaces were modelled as two-sided shell sheets of type finite conductivity, using the built-in material definition. Curvilinear elements were used for the adaptive meshing in combination with second-order basis functions. A minimum of two converged passes was required at 1 GHz, 2 GHz, 5 GHz, 7.5 GHz, and 10 GHz for a ΔS of 0.02. Finally, an interpolating sweep with 401 points over the range 0.1–10.1 GHz was used to obtain the simulation data. The dielectric performance of Ultem 1010 supplied by the manufacturer only covers a single frequency (1 kHz). Initial analysis of the same antenna design indicates that the higher frequency results did not match the simulation data [27]. Therefore, the material was characterised across the full frequency spectrum covered using the two-line method [28] with 25 mm and 50 mm microstrip transmission lines. The results from the characterization were then incorporated in ANSYS, which in turn led to the improved match between simulated and measured data presented here.

3.5. RF testing

The return loss performance of the antennas was measured using a FieldFox handheld microwave analyser (N9917A, Keysight). A single-port Short-Open-Load calibration was performed using a 3.5 mm mechanical calibration kit. The output power was set to −5 dBm, with an intermediate frequency bandwidth of 10 kHz. 401 points were measured over the range 0.1–10.1 GHz. The antennas were connected to the measurement equipment using flange SMA connectors soldered onto the capsules.

The radiation patterns of the capsule antennas were measured using an anechoic chamber. A 5-degree step was used, with the chamber calibrated for 0 dB reference level prior to the measurements and a double-ridged broadband horn antenna used as the source antenna. The radiation patterns were measured for $\theta = 90^\circ$ and $\varphi = [-180^\circ; +180^\circ]$.

The spiral inductors were measured using a vector network analyser (N9917A, Keysight). Two coils were separated at a distance of 10 mm apart and connected to the ports of the analyser. The inductance and power coupling were subsequently calculated from the S-parameters.

3.6. Positional and temperature sensor test setup

To measure the resistance of both sensor types, the devices were connected to a sourcemeter unit (2450, Keithley) in a 2-wire configuration. The temperature sensors were affixed to a metal plate with a K-Type thermocouple connected to a benchtop multimeter (2110 5½ Digit, Keithley) directly in contact with the sample. The setup was

loaded into an oven (LHT6030, Carbolite) and heated to 250 °C over 15 min. For positional and bend radius measurements, the samples were loaded into a linear compression rig with a 2D laser profilometer (ScanCONTROL 2900−50, Micro-Epsilon) mounted axially. The data logging and control of both setups was performed by a LabVIEW program that moved the rig at 20 mm/s with an accelerated of 200 mm/s. Initial testing of a single positional sensor demonstrated how environmental temperature impacted the measurement results [29]. Therefore, all positional testing presented in this paper was conducted in a temperature-controlled environment (20 °C ± 0.5 °C). In the future, an off-axis sensor could be fabricated to remove the effect of temperature on the positional sensing measurements.

4. Results and discussion

4.1. Conformal circuitry

The ability to pattern around 3D surfaces is demonstrated by patterning over a cylinder with a 1.75 mm radius (Fig. 2a). Using this new manufacturing strategy, electrical continuity was achieved on circuitry fabricated across conformal surfaces and 3D printed layers (Fig. 2b). White light interferometry demonstrates how on the microscale the circuitry bridges across the 3D printed surface artefacts (Fig. 2c) including the join between two infill paths. The volume conductivity of the electroless Cu at 20 °C was measured to be 3.73 × 107S/m ± 0.37 × 107S/m (mean ± standard deviation) for samples with a thickness of 559 nm ± 137 nm (Appendix A, Table A1). This value is 64.7 % of the handbook for bulk copper [34] and offers conductivity improvements over existing printed inks and pastes [1,4,35,36]. Additional galvanic and non-galvanic plating stages can also be carried out on the electroless Cu to expand the range of materials, deposit thicknesses and functionality of the patterned metallic features.

4.2. Solder reflow

Solder-based surface mount assembly (SMA) methods are extensively used in modern electronics manufacturing. During the reflow process the solder forms an intermetallic compound with the bond pad creating a strong and compliant attachment between the substrate and electronic component. Compared to typical 3D printable polymers, the PEI material has a higher glass transition temperature (T_g) (215 °C) and a low coefficient of thermal expansion (47 µm/m-°C) [31]. In addition, the ability to selectively metallize the polymer with electroless Cu provides a wettable surface for the solder. These combined properties allow miniaturized surface mount components to be reliably attached both mechanically and electrically to the substrate.

Initially a 555-timer circuit with flashing LED was manufactured to demonstrate the principles of a working circuit (Fig. 3a & Suppplementary Video 1). Test boards were then fabricated with pad configurations matching a range of commonly used SMA packaging formats including discrete components down to 0.6 mm × 0.3 mm in footprint and array interconnects with pitches down to 0.8 mm (Appendix C, Fig. C1). Using an atmospheric convection based reflow process, the most commonly employed solder paste for consumer goods, (Tin-Silver-Copper) was evaluated. This near eutectic solder alloy has a melt temperature similar to the T_g of the PEI substrate. However, due to the high heat deflection of PEI (216 °C) [31] and short peak temperature duration of the reflow process, no warping of the substrate was observed while achieving wetting of the solder to the bond pads (Fig. 3b). Comparable results were also found with a lower melting point solder (Tin-Bismuth). A range of SMA components (Fig. 3c) such as memory (Fig. 3d-i), processors (Fig. 3d-ii), inertial measurement units and passive devices such as capacitors and resistors (Fig. 3a-iii) were assembled on to this test board. This highly refined and robust surface mount interconnection method, previously out of the realms of 3D printing, will

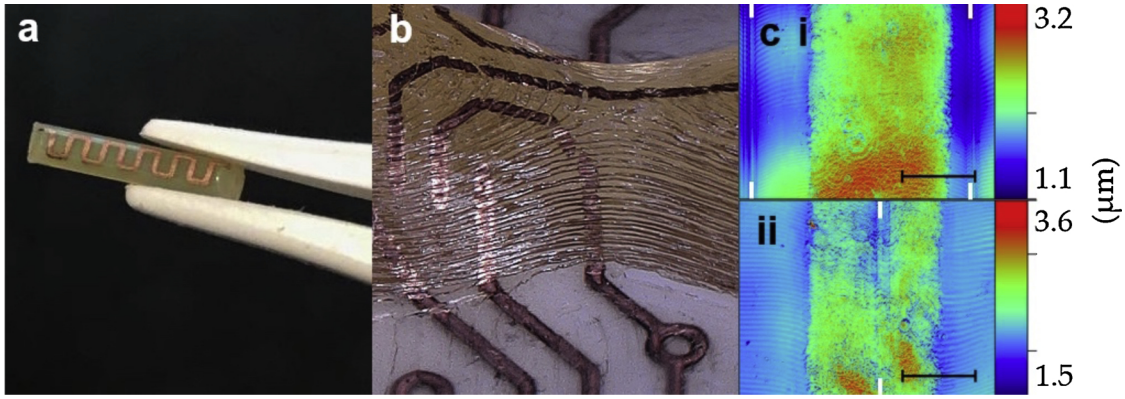

Fig. 2. Three-dimensional copper circuitry and surface mount assembly on polyetherimide substrates. **(a)** Selective metallization of a 1.75 mm diameter cylinder. **(b)** Conformal circuitry forming a continuous electrical pathway across the individual printed layers. **(c)** Cu metal traces covering **(i)** the centre of an infill path and **(ii)** the join between two infill paths (white markers indicate infill join point).

The minimum feature size achieved with the computer-controlled laser patterning system used in this research was 170 µm as a result of the laser spot size diameter. However, optical patterning methods have better lateral resolution when compared to traditional printing methods such as dispensing or jetting. To demonstrate the higher-resolution capability of this light-based patterning approach the same laser system was used to raster light over a chrome on glass photomask to synthesise Ag features approaching 10 µm on a round filament (Appendix B, Fig. B1). The use of more sophisticated digitally driven optical patterning systems could allow feature sizes approaching the theoretical Rayleigh criterion diffraction limit (λ/2). In addition to the field of electronics, the ability to directly synthesise metallic nanoparticles onto the surface of 3D printed parts allows new functionality including antimicrobial properties, catalytic surfaces and biochemical sensing [30].

facilitate devices that can operate at higher temperatures, withstand greater mechanical shock and provide excellent electrical signal performance.

4.3. Wireless communications and power transfer

The conductivity of the copper traces, coupled with the low relative permittivity (2.67) and small loss tangent (0.001) [31] of the substrate material, makes this process well-suited for high frequency communications and wireless power transfer applications. To showcase this capability a pill capsule antenna was designed, fabricated, and characterized (Fig. 4a). The pill diameter is 11 mm and height is 25 mm with a 0.4 mm conductor track width. The antenna patterned on the cylindrical surface comprises of two spiral monopoles, connected in

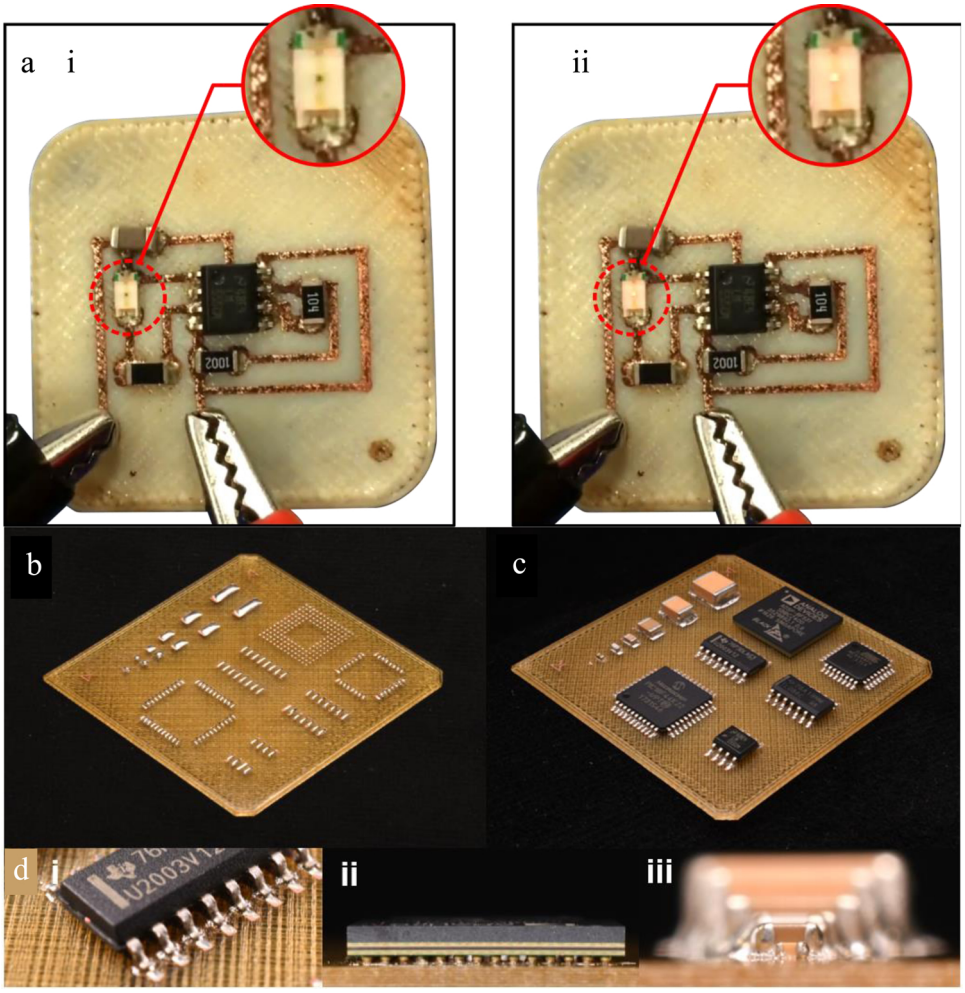

Fig. 3. Electronic packaging **(a)** 555 timer with flashing LED powered **(i)** LED off; **(ii)** LED on. **(b)** Solder reflowed surface mount test board. **(c)** Range of assembled surface mount components including capacitors from 5650 to 0603 (metric), a 160 pad mini-Ball Grid Array (mBGA), leaded Quad Flat Packages (QFP) and Small Outline Integrated Circuits (SOIC). **(d)** Close-ups of test board: **(i)** solder fillets on SOIC; **(ii)**, side view of mBGA; **(iii)**, series of capacitors increasing in size.

parallel, to ensure a wide solid angle coverage. The antenna was characterised over a broadband frequency range of 0.1–10 GHz, which covers many wireless communication standards including Wi-Fi, mobile phone (3 G, 4 G and 5 G) and all sub-6 GHz Industrial, Scientific and Medical frequency bands. There is very good agreement between measured and simulated results (Fig. 4b), with the broadband return

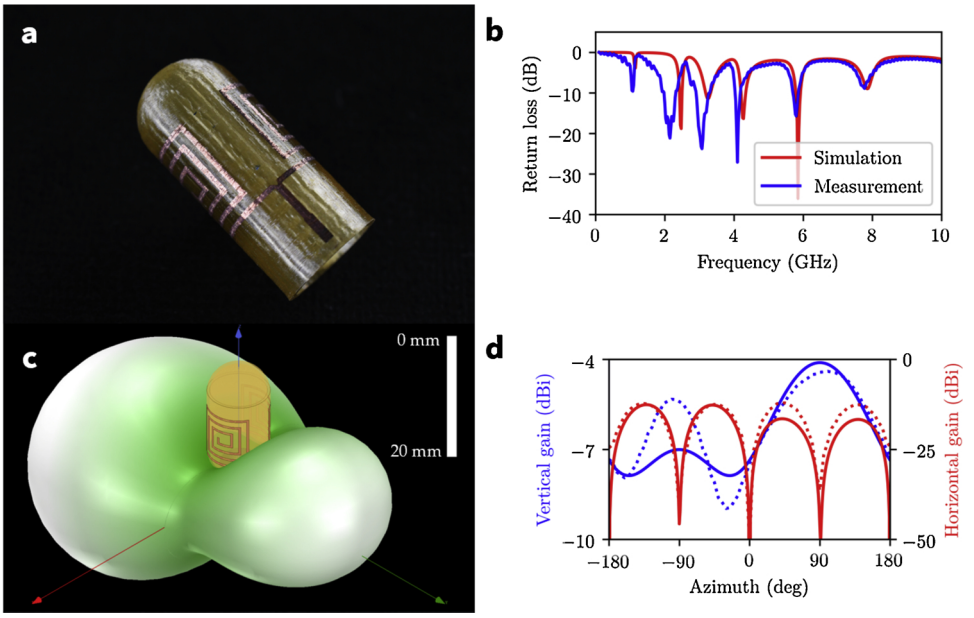

Fig. 4. Applications in high-frequency electronics. **(a)** Fabricated pill capsule antenna sample. **(b)** Comparison between measured and simulated return loss, showing multiple resonance frequencies. **(c)** Simulation model of pill capsule antenna with 3D radiation pattern at 1050 MHz. **(d)** Measured (dashed line) and simulated (solid line) radiation patterns for vertical and horizontal polarisation.

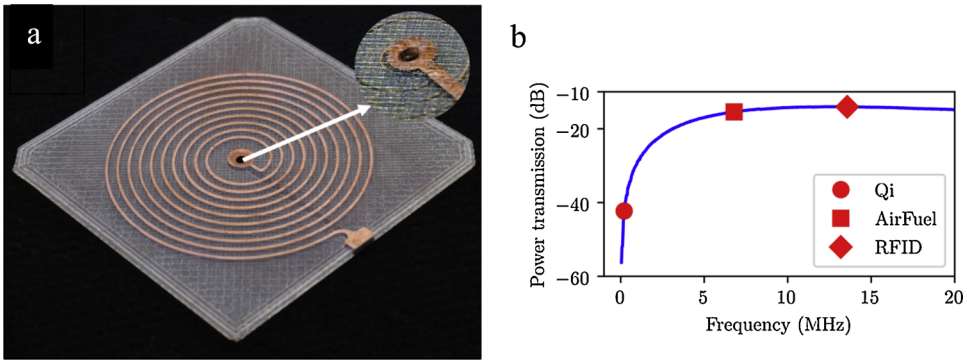

Fig. 5. Wireless power transfer. **(a)** Spiral RF coil with close-up of conductive via. **(b)** Power transmission between two coils at 10 mm distance.

loss exhibiting typical monopole behaviour and characteristic resonances at higher harmonic frequencies. A comparison between the simulated (Fig. 4c) and measured radiation pattern at the first resonant frequency of 1050 MHz for θ = 90°, φ = [-180°, +180°] (Fig. 4d) shows an excellent fit for both the horizontal and vertical polarisation radiation patterns. The differences between the simulated and measured return loss at the lower end of the measured frequency range can be explained by the parasitic effects from the SMA flange connector used to interface the pill capsule antennas with measurement equipment.

To test the principles of near-field wireless power transfer a pair of inductive planar RF coils were implemented as multi-turn spirals on one side of a 3D printed substrate, with a return track on the opposite side (Fig. 5a). This required the fabrication of a conductive through hole to form a vertical interconnect between both sides of the coils. Vias are also an essential feature for increasing the density of the electronic system by enabling double-sided and multilayer printed circuits. A demonstration of inductive power transfer between two coils spaced 10 mm apart (Fig. 5b) shows excellent level of coupling for two industry standard frequencies (6.78 MHz and 13.56 MHz). The coils also exhibited stable inductance (1.75 ± 0.25μH) over a broadband frequency range (50 kHz – 50 MHz), further making them suitable for use in applications such as wireless charging using Qi and AirFuel standards, and in HF RFID tags. Increasing the density of the coils by providing a higher turn ratio will improve the power transmission at the Qi standard frequency. The maximum achieved Q-factor, which is defined as $2\pi fL/R$, was around 4. This value is lower when compared to commercially available inductors, which is due to the high resistance caused by the low copper thickness (less than a micron). This can be resolved by using a different electroless plating solution designed to create thicker layers or using an electrolytic Cu plating process.

4.4. Flexible circuity and sensing

The layer-based approach of the FFF process allows localised control of the material thickness enabling tuneable stiffness of the polymer. Flexible substrates were created by depositing just two perpendicular 45 μm layers of PEI material. Using an electrochemical technique allows the creation of circuitry that can undergo a high degree of elastic deformation without breaking or detaching from the substrate (Fig. 6a). To assess the performance and reliability of the circuitry test pieces containing a 100 mm long track were fabricated. The samples were flexed from a straight position to a minimum 6.59 mm bend radius for 50,000 cycles to experimentally validate the adhesion, ductility and fatigue life of the fabricated electronic substrates. All 6 devices functioned mechanically and electrically throughout the testing and exhibited minimal drift in measured circuit resistance (< 1%) (Fig. 6b). These results demonstrate how a combined approach avoids the limitations of directly printing the conductor material and allows conformal metalized features to be generated which are strongly adhered to the 3D surface.

The collective material properties of the polymer layers and selective metal patterns allowed using this process to manufacture resistive-based sensors which exhibit stable performance across a range of conditions. Since the resistivity of the bulk Cu conductor material changes as a function of temperature electrodes were fabricated and the response measured from ambient conditions to 175 °C. A linear 0.0025/°C temperature coefficient of resistance was observed across 5 samples (Fig. 6c). To further exploit the ability to produce bendable functionalised 3D printed structures, flexible positional sensors capable of a tight bend radius with a long fatigue life were manufactured (Fig. 6d). A linear buckling rig compressed the sensors axially by 5 mm in 1.25 mm increments and monitored both deflection and resistance. Over 20,000 cycles the samples showed no degradation mechanically and produced a measurable change in R/R_0 without re-calibration (Fig. 6e). The freeform nature of this process allows future consideration for the fabrication of customized 3D sensor arrays. In addition, the chemical inertness of the substrate, the ability to plate other types of metals and the capability for surface mount assembly of micro-electromechanical systems facilitates future avenues for implementing a diverse range of sensing methods.

4.5. Actuation

For the development of self-folding electronics, motorless actuation approaches using smart materials offers a potentially lightweight, compact and quiet alternative for generating movement within 3D printed structures [32,33]. To test this principle, a device was created through the selective printing of high and low flexibility segments; patterning of metal heating elements; and the embedding of shape memory alloy wire (SMA) (Fig. 7a). SMAs are metallic compounds that exhibit both superelasticity and shape recovery during a heating cooling cycle. With Joule heating, the current is passed directly through the nitinol wire to induce heating whereby indirect heating uses a secondary heat source. The indirect heating method overcomes some of the challenges connecting to the nitinol making it easier to selectively actuation regions of wire (Fig. 7b). This is demonstrated by the creation of a three-segment folding structure that can be controlled to eight discrete positions (Fig. 7c). The high T_g of this thermoplastic polymer and the bulk Cu material allows heating element temperatures that can approach 200 °C to facilitate rapid heat transfer to the SMA wire. Bi-directional movement can also be achieved through the incorporation of antagonistic actuators, springs or utilising the variable stiffness of the printed structures.

5. Conclusions

This paper has presented a new technique for the production of rigid and flexible 3D electronic circuitry that exhibit excellent thermal, mechanical, and electromagnetic characteristics. The digitally driven

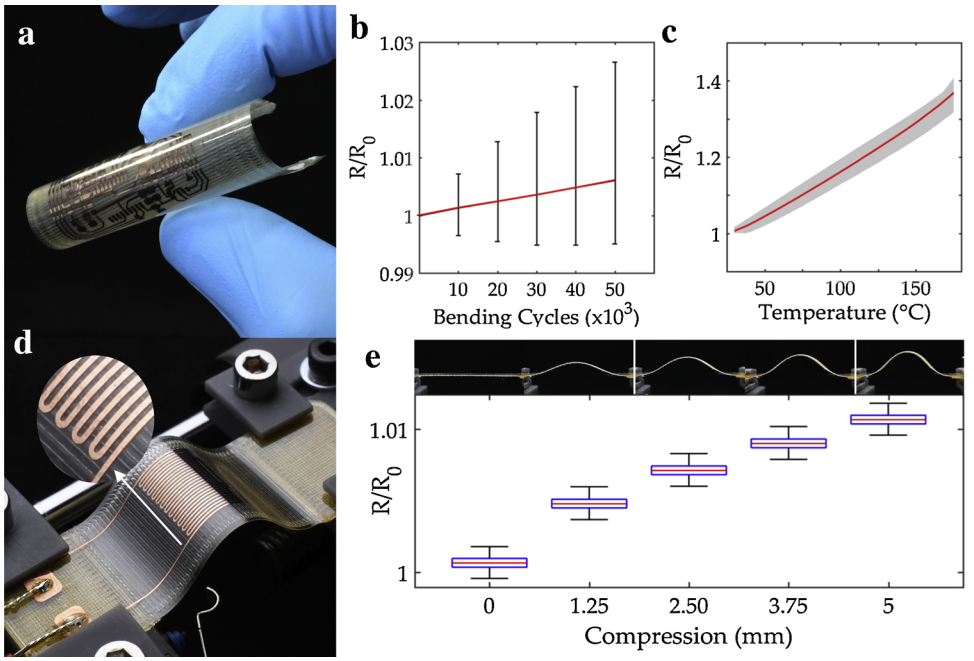

Fig. 6. Flexible electronics and sensing. **(a)** Highly ductile circuitry patterned onto a 90 μm thick substrate. **(b)** six samples compressively cycled 50,000 times to a 6.59 mm bend radius showing no electrical failure and stable resistivity. **(c)** Average resistance response of temperature sensors. **(d)** Combined rigid and flexible circuitry to fabricate a positional sensor. **(e)** Normalised resistance over 20,000 cycles for a positional sensor compressed in 1.25 mm increments.

nature of this process enables new designs freedoms through the precise spatial control of high performance conductive and dielectric materials. This work demonstrates how closer integration of mechanical and electronic systems can be achieved through embedded actuation, sensing, power transfer, data processing and communications. The ability to solder surface mount components offers a route to achieving the reliability of modern electronic systems whilst enabling the transition to complex 3D printed architectures. Incorporation of movement within these functional structures allows designers to consider how to build active origami, auxetic and bioinspired designs. The chemical modification and light-based patterning approach overcomes many of the limitations of direct printing methods particularly in relation to conductivity, resolution and adhesion of the conductor layers. Furthermore, these results can be achieved using a combination of low-cost, commercially available filaments, printers, and optical patterning equipment with minor modifications. The overall resolution and performance of this new manufacturing approach opens up routes to produce mass-customised medical devices, personalized wearable technology and bespoke robotic systems.

Contributions

R.W.K conceived the idea of combining M.P.Y.D and J.M-H research for selectively metalizing 'imide' based polymers with FFF printing to develop a fully digitally driven manufacturing process. R.W.K supervised the overall work conducted in this research paper.

R.N.E & M.P.S jointly developed the manufacturing apparatus and experiments to validate this digitally driven approach under the supervision of R.A.H and R.W.K.

V.D. designed, simulated and tested all the RF devices under I.D.R supervision. N. J. W. supported the selective actuation, sensing, and packaging aspect of this research.

N. J. W. also conducted a detailed literature review for this paper. J.H. conducted the surface mount packaging including solder

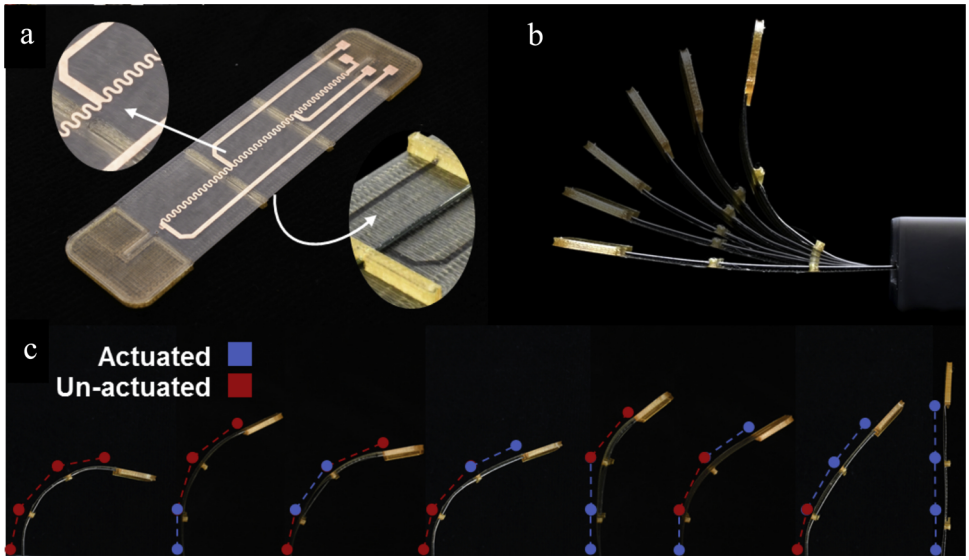

Fig. 7. Selective actuation circuit using 3 individually addressable heating elements. **(a)** Nitinol wire is embedded within the substrate. **(b)** Time-lapse showing full range of motion. **(c)** Various sections individually actuated to 8 discrete positions.

dispensing, pick and place assembly and solder reflow.

J.M-H, T.D.A.J and A.R. contributed to chemical modification process under the supervision of M.P.Y.D. and J.M-H. and discovered a method to amplify the process alongside validating the underpinning chemistry as further detailed in reference [26].

Declaration of Competing Interest

The authors declare that they have no known competing financial interests or personal relationships that could have appeared to influence the work reported in this paper.

Acknowledgements

The authors thank the Engineering & Physical Sciences Research Council (EPSRC) for their financial support under the grants Photobioform I (Grant NumbersEP/L022192/1 andEP/L022133/1), Photobioform II (Grant NumbersEP/N018222/1 andEP/N018265/2).

Appendix A. Copper Thickness Measurements

The thickness of the copper was estimated by taking a plane fit across a series of 0.4 mm wide Cu tracks. The position of the reference surface was measured at the base of the step change on each side of the copper trace. The mean of these values was then compared to the height across the centre 200 μm of the trace to determine the approximate thickness of the copper.

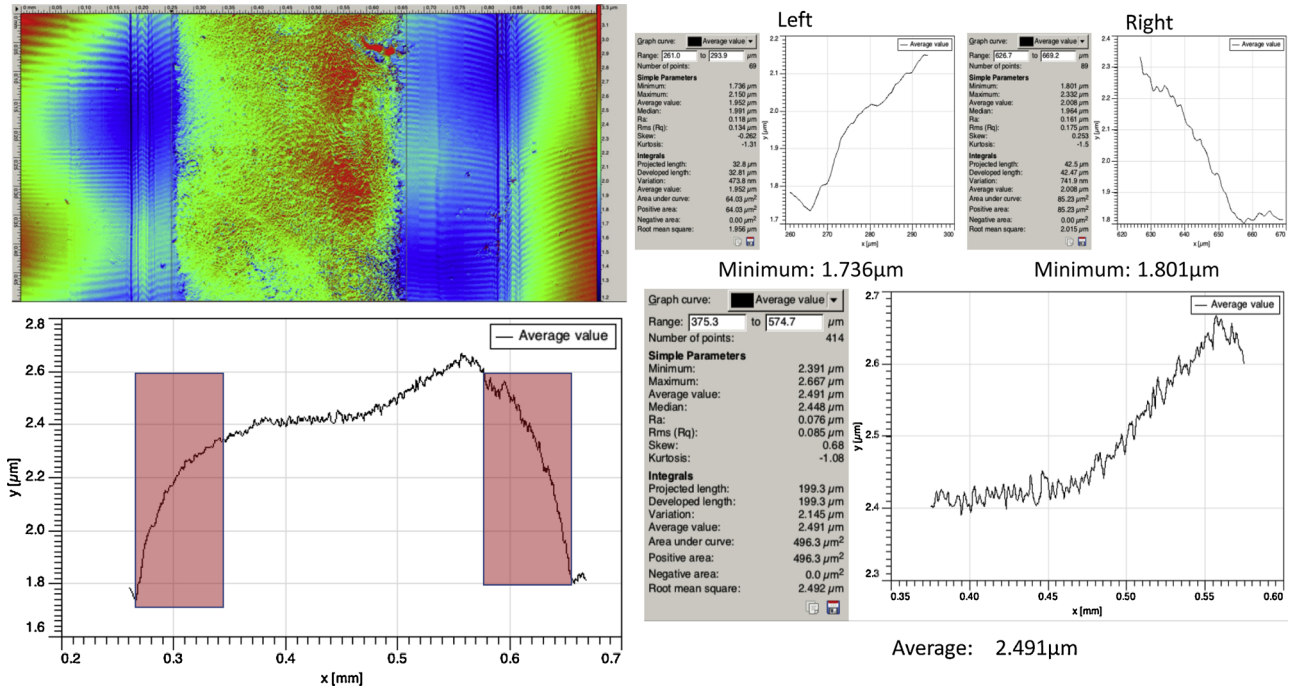

Fig. A1. Method for determining Cu track height.

Table A1
Cu Thickness measurements.

Sample	Avg. Cu (μm)	Min. Left (μm)	Min. Right (μm)	Avg. Min (μm)	Step Height (μm)
1	2.257	1.727	1.749	1.738	0.519
2	2.474	2.109	2.099	2.104	0.370
3	3.182	2.41	2.671	2.540	0.642
4	2.460	1.75	1.558	1.654	0.806
5	2.358	1.699	1.804	1.752	0.607
6	2.213	1.644	1.747	1.696	0.518
7	2.311	1.876	1.801	1.839	0.473
8	0.205	−0.195	−0.189	−0.192	0.397
9	2.491	1.736	1.801	1.769	0.723
10	2.258	1.74	1.705	1.723	0.536
				Mean (μm)	0.559
				Std. Dev. (μm)	0.137

Appendix B. 10 μm Silver Nanoparticle Formation

A horizontal micrometer transmission recticle (75 mm × 25 mm × 1.5 mm) was used as a photomask to reduce the limitation of the laser spot size. The micrometer markings are 10 μm wide at 50 μm pitch. A 1.75 mm diameter Ultem 1010 filament was placed into contact with the chrome patterned side of the mask and exposed to 350 J/cm^2 irradiation. As the recticle is designed for transmission viewing on a microscope the projected pattern is mirrored through exposure. The round shape of the filament results in the projected exposure pattern to be diffracted causing the features to enlarge when moving away from the contact zone on the mask. Prior to SEM imaging the samples were coated with a thin iridium layer using a sputter coater to reduce the polymer layer charging.

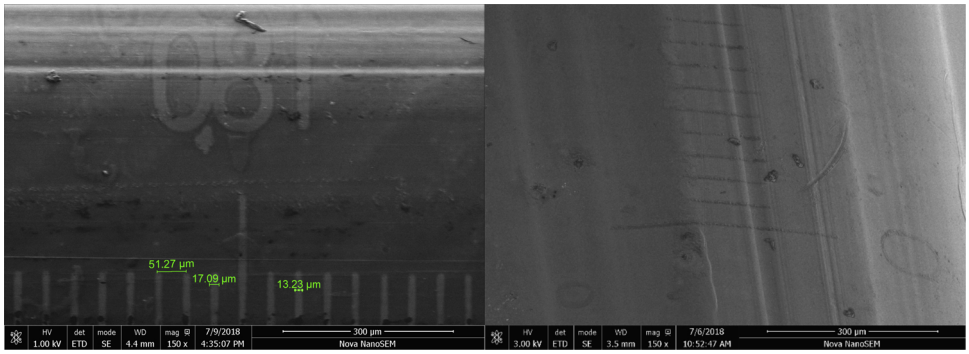

Fig. B1. Scanning Electron Microscope image showing Ag features on a cylinder patterned down to 13.23 μm.

Appendix C. Surface Mount test board layout

List of SMD component sizes:

1 2220 SMD – 5.7 mm × 5 mm
2 1812 SMD – 4.6 mm × 3.2 mm
3 1210 SMD – 3.2 mm × 2.5 mm
4 0805 SMD – 2.8 mm × 1.9 mm
5 0603 SMD – 1.55 mm × 0.85 mm
6 0402 SMD – 1.2 mm × 0.6 mm
7 0201 SMD – 0.6 mm × 0.3 mm
8 160 Pad CSPBGA – 0.8 mm pitch
9 16 Pad SOIC – 1.27 mm pitch
10 44 Pad TQFP – 0.8 mm pitch
11 32 Pad TQFP – 0.8 mm pitch
12 14 Pad SOIC – 1.27 mm pitch
13 8 Pad SOIC – 1.27 mm pitch

Acronyms: Surface Mount Device (SMD), Chip-Scale Package Ball Grid Array (CSPBGA), Small Outline Integrated Circuit (SOIC), Thin Quad Flat Package (TQFP)

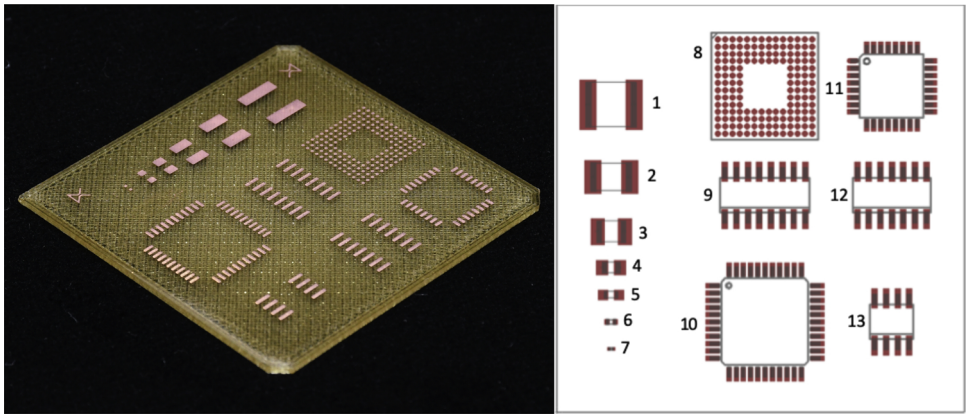

Fig. C1. (left): image of Cu bond pads, (right) Component pad layout.

Appendix D. Supplementary data

Supplementary material related to this article can be found, in the online version, at doi:https://doi.org/10.1016/j.addma.2020.101367.

References

[1] E. MacDonald, R. Wicker, Multiprocess 3D printing for increasing component functionality, Science 353 (2016), https://doi.org/10.1126/science.aaf2093 aaf2093.

[2] G.Z. Yang, J. Bellingham, P.E. Dupont, P. Fischer, L. Floridi, R. Full, N. Jacobstein, V. Kumar, M. McNutt, R. Merrifield, B.J. Nelson, B. Scassellati, M. Taddeo, R. Taylor, M. Veloso, Z.L. Wang, R. Wood, The grand challenges of science robotics, Sci. Robot. 3 (2018), https://doi.org/10.1126/scirobotics.aar7650 eaar7650.

[3] J. Lee, H.-C. Kim, J.-W. Choi, I.H. Lee, A review on 3D printed smart devices for 4D printing, Int. J. Precis. Eng. Manuf. Technol. 4 (2017) 373–383, https://doi.org/10.1007/s40684-017-0042-x.

[4] P.F. Flowers, C. Reyes, S. Ye, M.J. Kim, B.J. Wiley, 3D printing electronic components and circuits with conductive thermoplastic filament, Addit. Manuf. (2017), https://doi.org/10.1016/j.addma.2017.10.002.

[5] K. Sun, T.S. Wei, B.Y. Ahn, J.Y. Seo, S.J. Dillon, J.A. Lewis, 3D printing of interdigitated Li-ion microbattery architectures, Adv. Mater. 25 (2013) 4539–4543, https://doi.org/10.1002/adma.201301036.

[6] J.A. Lewis, Direct ink writing of 3D functional materials, Adv. Funct. Mater. 16 (2006) 2193–2204, https://doi.org/10.1002/adfm.200600434.

[7] J. Li, Y. Wang, G. Xiang, H. Liu, J. He, Hybrid additive manufacturing method for selective plating of freeform circuitry on 3D printed plastic structure, Adv. Mater. Technol. 4 (2019) 1800529, , https://doi.org/10.1002/admt.201800529.

[8] J. Li, T. Wasley, T.T. Nguyen, V.D. Ta, J.D. Shephard, J. Stringer, P. Smith, E. Esenturk, C. Connaughton, R. Kay, Hybrid additive manufacturing of 3D electronic systems, J. Micromech. Microeng. 26 (2016) 105005, , https://doi.org/10.1088/0960-1317/26/10/105005.

[9] A. Joe Lopes, E. MacDonald, R.B. Wicker, Integrating stereolithography and direct print technologies for 3D structural electronics fabrication, Rapid Prototyp. J. 18 (2012) 129–143, https://doi.org/10.1108/13552541211212113.

[10] W. Zhou, F.A. List, C.E. Duty, S.S. Babu, Fabrication of conductive paths on a fused deposition modeling substrate using inkjet deposition, Rapid Prototyp. J. (2016), https://doi.org/10.1108/RPJ-05-2014-0070.

[11] S. Zips, O.J. Wenzel, P. Rinklin, L. Grob, K. Terkan, N.Y. Adly, L. Weiß, B. Wolfrum, Direct stereolithographic 3D printing of microfluidic structures on polymer substrates for printed electronics, Adv. Mater. Technol. (2019), https://doi.org/10.1002/admt.201800455.

[12] J.A. Paulsen, M. Renn, K. Christenson, R. Plourde, Printing conformal electronics on 3D structures with aerosol jet technology, 2012 Futur. Instrum. Int. Work. Proc. IEEE, 2012, pp. 1–4, , https://doi.org/10.1109/FIIW.2012.6378343.

[13] A. Mahajan, C.D. Frisbie, L.F. Francis, Optimization of aerosol jet printing for high-resolution, high-aspect ratio silver lines, ACS Appl. Mater. Interfaces 5 (2013) 4856–4864, https://doi.org/10.1021/am400606y.

[14] E. Macdonald, D. Espalin, D.W. Muse, R.B. Wicker, 3D Printing multifunctionality: Structures with electronics, Artic. Int. J. Adv. Manuf. Technol. (2014), https://doi.org/10.1007/s00170-014-5717-7.

[15] C. Kim, D. Espalin, A. Cuaron, M.A. Perez, M. Lee, E. MacDonald, R.B. Wicker, Cooperative tool path planning for wire embedding on additively manufactured curved surfaces using robot kinematics, J. Mech. Robot. 7 (2015) 021003, , https://doi.org/10.1115/1.4029473.

[16] P. Amend, C. Pscherer, T. Rechtenwald, T. Frick, M. Schmidt, A fast and flexible method for manufacturing 3D molded interconnect devices by the use of a rapid prototyping technology, Phys. Procedia 5 (2010) 561–572, https://doi.org/10.1016/j.phpro.2010.08.084.

[17] H. Ota, S. Emaminejad, Y. Gao, A. Zhao, E. Wu, S. Challa, K. Chen, H.M. Fahad, A.K. Jha, D. Kiriya, W. Gao, H. Shiraki, K. Morioka, A.R. Ferguson, K.E. Healy, R.W. Davis, A. Javey, Application of 3D printing for smart objects with embedded electronic sensors and systems, Int. J. Adv. Mater. Technol. 1 (2016) 1600013, , https://doi.org/10.1002/admt.201600013.

[18] J.P. Swensen, L.U. Odhner, B. Araki, A.M. Dollar, Printing three-dimensional electrical traces in additive manufactured parts for injection of low melting temperature metals, J. Mech. Robot. 7 (2015) 021004, , https://doi.org/10.1115/1.4029435.

[19] S.Y. Wu, C. Yang, W. Hsu, L. Lin, 3D-printed microelectronics for integrated circuitry and passive wireless sensors, Microsystems Nanoeng. (2015), https://doi.org/10.1038/micronano.2015.13.

[20] B.S. Yim, Y. Kwon, S.H. Oh, J. Kim, Y.E. Shin, S.H. Lee, J.M. Kim, Characteristics of solderable electrically conductive adhesives (ECAs) for electronic packaging, Microelectron. Reliab. (2012), https://doi.org/10.1016/j.microrel.2011.12.004.

[21] N. Lazarus, S.S. Bedair, S.H. Hawasli, M.J. Kim, B.J. Wiley, G.L. Smith, Selective electroplating for 3D-Printed electronics, Int. J. Adv. Mater. Technol. 4 (2019) 1–5, https://doi.org/10.1002/admt.201900126.

[22] M.J. Kim, M.A. Cruz, S. Ye, A.L. Gray, G.L. Smith, N. Lazarus, C.J. Walker, H.H. Sigmarsson, B.J. Wiley, One-step electrodeposition of copper on conductive 3D printed objects, Addit. Manuf. 27 (2019) 318–326, https://doi.org/10.1016/j.addma.2019.03.016.

[23] S. Ikeda, K. Akamatsu, H. Nawafune, Direct photochemical formation of Cu patterns on surface modified polyimide resin, J. Mater. Chem. 11 (2001) 2919–2921, https://doi.org/10.1039/b107386a.

[24] K. Akamatsu, S. Ikeda, H. Nawafune, Site-selective direct silver metallization on surface-modified polyimide layers, Langmuir 19 (2003) 10366–10371, https://doi.org/10.1021/la034888r.

[25] D.E. Watson, J.H.G. Ng, K.E. Aasmundtveit, M.P.Y. Desmulliez, In-situ silver nanoparticle formation on surface-modified polyetherimide films, IEEE Trans. Nanotechnol. 13 (2014) 736–742, https://doi.org/10.1109/TNANO.2014.2318203.

[26] J. Marques-Hueso, T.D.A. Jones, D.E. Watson, A. Ryspayeva, M.N. Esfahani, M.P. Shuttleworth, R.A. Harris, R.W. Kay, M.P.Y. Desmulliez, A Rapid Photopatterning Method for Selective Plating of 2D and 3D Microcircuitry on Polyetherimide, Adv. Funct. Mater. 28 (2018) 1704451, , https://doi.org/10.1002/adfm.201704451.

[27] M.R.N. Esfahani, M.P. Shuttleworth, R.A. Harris, R.W. Kay, V. Doychinov, I.D. Robertson, J. Marques-Hueso, T.D.A. Jones, A. Ryspayeva, M.P.Y. Desmulliez, Hybrid additive manufacture of conformal antennas, 2018 IEEE MTT-S Int. Microw. Work. Ser. Adv. Mater. Process. RF THz Appl. IMWS-AMP 2018, 2018, https://doi.org/10.1109/IMWS-AMP.2018.8457128.

[28] M.Q. Lee, S. Nam, An accurate broadband measurement of substrate dielectric constant, IEEE Microw. Guid. Wave Lett. (1996), https://doi.org/10.1109/75.481077.

[29] M.P. Shuttleworth, M.N. Esfahani, J. Marques-Hueso, T.D.A. Jones, A. Ryspayeva, M.P.Y. Desmulliez, R.A. Harris, R.W. Kay, A New digitally driven process for the fabrication of integrated flex-rigid electronics, Proc. 29th Annu. Int. Solid Free. Fabr. Symp. (2018).

[30] A. Schröfel, G. Kratošová, I. Šafařík, M. Šafaříková, I. Raška, L.M. Shor, Applications of biosynthesized metallic nanoparticles - A review, Acta Biomater. (2014), https://doi.org/10.1016/j.actbio.2014.05.022.

[31] Stratasys Ltd., ULTEM 1010 Resin, datasheet, 2015. http://usglobalimages.stratasysLtd.com/Main/Files/Material_Spec_Sheets/MSS_FDM_ULTEM1010.pdf (accessed September 16, 2018).

[32] S. Felton, M. Tolley, E. Demaine, D. Rus, R. Wood, A method for building self-folding machines, Science 345 (80-) (2014) 644–646, https://doi.org/10.1126/science.1252610.

[33] S.M. Felton, M.T. Tolley, B. Shin, C.D. Onal, E.D. Demaine, D. Rus, R.J. Wood, Self-folding with shape memory composites, Soft Matter 9 (2013) 7688–7694, https://doi.org/10.1039/c3sm51003d.

[34] R.A. Matula, Electrical resistivity of copper, gold, palladium, and silver, J. Phys. Chem. Ref. Data 8 (1979) 1147–1298, https://doi.org/10.1063/1.555614.

[35] A.J. Lopes, I.H. Lee, E. Macdonald, R. Quintana, R.B. Wicker, Laser curing of silver-based conductive inks for in situ 3D structural electronics fabrication in stereolithography, J. Mater. Process. Technol. 214 (2014) 1935–1945, https://doi.org/10.1016/j.jmatprotec.2014.04.009.

[36] B. Urasinska-Wojcik, N. Chilton, P. Todd, C. Elsworthy, M. Bates, G. Roberts, G.J. Gibbons, Integrated manufacture of polymer and conductive tracks for real-world applications, Addit. Manuf. 29 (2019) 100777, https://doi.org/10.1016/j.addma.2019.06.028.